Journal of JSCE, Vol. 11, No. 2, 22-15025, 2023.

EULERIAN-LAGRANGIAN APPROACH FOR INTERACTIONS BETWEEN FLUIDS AND MULTIPLE DEFORMABLE SWELLING OBJECTS USING MASS-SPRING MODEL

Niku GUINEA[1], Daisuke TORIU[2] and Satoru USHIJIMA[3]

[1]Nonmember of JSCE, Graduate School of Engineering, Kyoto University-Katsura
(Nishikyo-ku, Kyoto. 615-8540)
E-mail: guinea.niku.25w@st.kyoto-u.ac.jp (Corresponding Author)
[2]Member of JSCE, Academic Center for Computing and Media Studies, Kyoto University
(Yoshida-Honmachi, Sakyo-ku Kyoto. 606-8501)
E-mail: toriu.daisuke.8v@kyoto-u.ac.jp
[3]Member of JSCE, Academic Center for Computing and Media Studies, Kyoto University
(Yoshida-Honmachi, Sakyo-ku Kyoto. 606-8501)
E-mail: ushijima.satoru.3c@kyoto-u.ac.jp

A computation method was proposed for the interactions between Newtonian fluids and deformable solid objects which swell by absorbing the surrounding fluids. The direct-forcing immersed boundary method and mass-spring model are used to estimate the fluid-solid interactive forces and deformations of the solid. The swelling of the object is simulated by changing the natural lengths of the spring models. In addition, the solid-solid interaction is treated by utilizing the distinct element method. The proposed method was applied to three numerical experiments. As a result, it was shown that the basic behaviors of the swelling-deformable objects are reasonably calculated with the present method.

Key Words: *Fluid-solid interaction, Swelling, Deformable object, Immersed boundary method, Mass-spring model*

1. INTRODUCTION

The main target in this study is on the computational method for the interactions between Newtonian fluids and swelling deformable solid objects. Swelling, a process where solid objects expand as they absorb fluids especially in liquid form, can be found in many natural materials such as clays,[1)] food gels,[2)] biological tissues,[3)] and industrial materials such as absorbent polymers in hygienic products,[4)] and preformed particle gel used in water shutoff treatment,[5)] and hydrogel.[6)] In industrial materials, such swelling polymers are commonly made from Super Absorbent Polymer (SAP). When modeling such objects, there are four important points to be considered: (1) interaction between the fluid and objects, (2) deformation of the objects, (3) solid interaction (contact) between objects, and (4) absorption and size increase of the objects.

In some conditions these 4 points affect each other. Such phenomenon is reported by Jockusch et al.[7)] When fluid flow on a bed of SAP particles, the swelling on the upper layer inhibits the fluid flow and absorption of fluid in the lower parts. This is caused by the deformation of SAP particles which decreases the porosity of the bed of SAP particles on the top layer. Another study on mixture of soil and SAP particles used in agriculture fields by Misiewicz et al[8)] reports how the swelling rate of SAP particles is also influenced by the pressure deformation. Higher pressure by coarser soil surrounding the SAP particles are reported to reduce the swelling rate compared to when fine-grained soil are mixed.

In our investigation, very few studies focus on the all 4 points. Some of the studies are focusing only on the combination between the 4 points to make the computation simple, such as a study employing a macro-scale model to investigate the behavior of a bed of swelling SAP particles[9),10)] (focusing on point (1), (2), and (4)), a study using a grain-scale model based on the Discrete Element Method (DEM) and pore finite volume method[11)] (points (3) and (4)), and a study of absorbent particles in free-surface flows[12)] (points (1) and (4)).

In order to be able to reproduce the closest con-

dition to this complicated phenomena, a method that is able to simulate the 4 main processes is proposed in this study. A coupling of the Direct Forcing Immersed Boundary (DF/IB) method and Mass-Spring Model (MSM) is used to solve points (1) and (2). The mass-spring model[13] is one useful method used to predict the deformation of the solid due to its simplicity and low computational cost. In recent years, various applications of the mass-spring model were studied such as in cloth simulations[14][15]and soft tissues simulations.[16][17][18] While the coupled DF/IB and Mass-Spring Model (MSM-DF/IB) is simple and has low computational cost, the method shows reasonable results for the computation.[19][20]

In the computation of DF/IB, multiple Lagrangian points are arranged on the solid surface to calculate the fluid-solid interaction forces. In the proposed method, a different DF/IB scheme from the original DF/IB for rigid bodies[21] is used. Instead of solving the equation of motion for the center point of the rigid body using the total value of fluid-solid interaction forces, the motion is calculated separately on each Lagrangian point. The same Lagrangian points are also used for the calculation of the mass-spring model. The mass (Lagrangian) points are connected with springs and dashpot which compress and extend as the objects deform. In addition, when contact between solid objects is considered (point (3)), the implementation of the DEM[22] for the computation is fairly easy as the same points is used for the placement of the Contact Detection Spheres (CDS). The CDS are treated as rigid bodies that are connected by the springs. Additionally, in order to simulate point (4), the natural length of the spring used in the mass-spring model is utilized in the proposed method to predict the swelling of the particle with respect to time.

The proposed method of MSM-DF/IB with a swelling scheme is applied to three applications. First, the method's capability to predict the swelling of a hydrogel particle is checked. Several hydrogel particles are first observed and the diameter growth is recorded. The relation between diameter and time is obtained and used in the computation and the results are compared with the experimental data. Second, the proposed method is compared to the original DF/IB for rigid body and references by calculating the sedimentation of a single particle in the fluid. The swelling scheme is then introduced and the results of the computations are discussed. In the third application, the proposed method is applied to lid-driven cavity flow with non-swelling multiple deformable objects and swelling multiple deformable swelling objects. The results of the computations between two values of spring constant are compared and the deformations and basic swelling behaviors of the objects are discussed.

2. NUMERICAL METHODS

(1) Fluid Computations with DF/IB

DF/IB method proposed by Uhlmann[21] is used for the computation of the fluid-solid interactions. The governing equations for incompressible fluids are first solved to obtain the tentative fluid velocities assuming that fictitious fluid exists inside the solid which is considered as deformable body in this study. The details of the computations are also explained in details by Guinea.[19]

Firstly, the incompressible condition and the momentum equations of the fluid are given by

$$\frac{\partial u_j}{\partial x_j} = 0, \tag{1}$$

$$\frac{\partial u_i}{\partial t} + \frac{\partial (u_i u_j)}{\partial x_j} = -\frac{1}{\rho_f}\frac{\partial p}{\partial x_i} + \nu \frac{\partial^2 u_i}{\partial x_j^2} + f_i + \lambda_i, \tag{2}$$

where u_j is the velocity component in x_j direction in two-dimensional Cartesian coordinates. where t is time, x_i is the component of Cartesian coordinate system, ρ_f is density, ν is kinematic viscosity, and p is pressure. In addition, u_i is the velocity component, f_i and λ_i are the external and fluid interaction forces in x_i direction. Note that the equations are written in Einstein notation. The governing equations are discretized with a finite volume method on the collocated grid system and solved using SMAC method.[23]

The deformable solid objects with circular shapes in the initial condition are calculated in the 2D field. The settings used in the computation of solid objects are shown in Fig. 1. Figure 1 (a) shows the Lagrangian points used in DF/IB for the computations of fluid-solid interactions. In the immersed boundary method, the fluid cells are set on the whole computational domain that contains the solid domain. The Lagrangian points that arranged on the swelling solid boundary move on the fluid cells, and the solid domain is fictitiously filled with fluid in the proposed method. Figure 1 (b) shows the multiple mass points of the objects, and Fig. 1 (c) shows the contact detection spheres used in contact calculation between multiple objects.

In DF/IB calculation, tentative velocities on the Eulerian cells in the prediction stage are first interpolated into Lagrangian points arranged on the solid surface using a discrete delta function. The fluid interaction force is then calculated on each Lagrangian point and spread back into Eulerian cells. The value of tentative velocity on Eulerian cells are then updated with the fluid interaction forces. As the computations of the DF/IB are the same with the previous study,[19] the details will be omitted on this paper. The flowchart for the fluid computations with DF/IB can be seen on

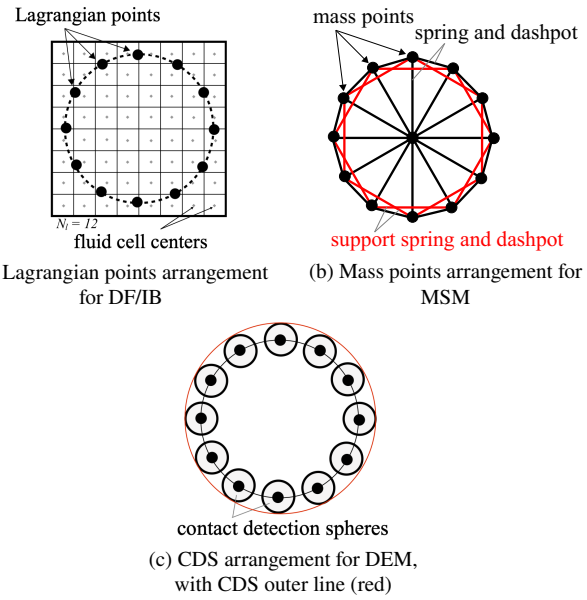

(a) Lagrangian points arrangement for DF/IB

(b) Mass points arrangement for MSM

(c) CDS arrangement for DEM, with CDS outer line (red)

Fig. 1 Schematic of (a) fluid cells and Lagrangian points for DF/IB, (b) mass-spring model, and (c) CDS[19)]

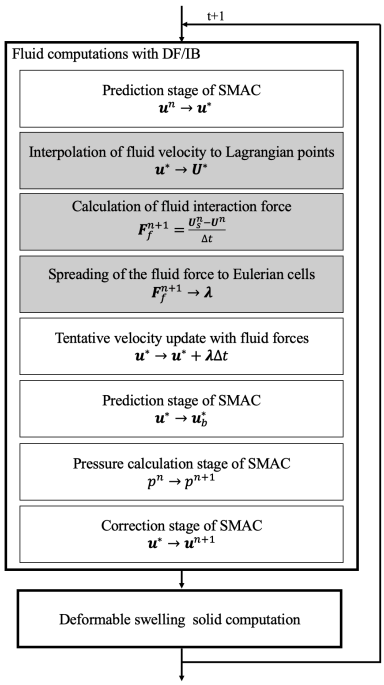

Fig. 2 Flowchart of the fluid computations with DF/IB

Fig. 2. The white blocks indicate that the computations are taking place on Eulerian cells and the grey blocks indicate that the computations are taking place on Lagrangian points.

(2) Mass-Spring Model for Deformable Swelling Solid

The motions of each Lagrangian point are solved separately considering the addition of spring-damping forces, contact forces, and external forces. Since each point on the surface can move freely, we can predict the deformation of the objects. where $\boldsymbol{U}_s$ is the vector of the mass point velocity, and the dot sign represents the time derivation. M is the mass of each Lagrangian point given by $M = \rho_s V_s / N_l$, where ρ_s is the solid density, V_s is the volume of the solid object, and N_l is the number of mass points (Lagrangian points). $\boldsymbol{F}_s$ is the vector of the force calculated by the spring-dashpot model, $\boldsymbol{F}_f$ is the vector of the fluid forces calculated with DF/IB, $\boldsymbol{F}_c$ is the vector of the contact force calculated with contact detection spheres and DEM, and $\boldsymbol{F}_e$ is the vector of the external forces.

Black and red lines in Fig. 1 (b) represent springs and dashpots between mass points. As a swelling model is proposed, the computation of the spring forces is a little bit different than the previous study. The spring and damping forces $\boldsymbol{F}_{s,AB}$ between two points A and B are calculated as shown in

$$\begin{aligned} \boldsymbol{F}_{s,AB} = &-k_s \left(\xi_{AB}^n - L_{AB}^n\right) \boldsymbol{n}_{AB} \\ &+c_s \left(\boldsymbol{U}_{s,A} - \boldsymbol{U}_{s,B}\right). \end{aligned} \tag{3}$$

Here, ξ_{AB} is calculated as $\|\boldsymbol{X}_A - \boldsymbol{X}_B\|$ and L_{AB} is the natural length of the spring between two points A and B. The details of L_{AB} will be explained in the next subsection. Furthermore, k_s is the spring stiffness constant and c_s is the damping coefficient. The damping coefficient used in the proposed method is calculated using

$$c_s = 2\sqrt{\left(\frac{M k_s \left(\ln e_b\right)^2}{\pi^2 + \left(\ln e_b\right)^2}\right)}, \tag{4}$$

where e_b is the coefficient of restitution which represents the ratio of relative velocity after and before collision. Additionally, $\boldsymbol{n}_{AB}$ is the unit normal vector given by

$$\boldsymbol{n}_{AB} = \frac{\boldsymbol{X}_A - \boldsymbol{X}_B}{\|\boldsymbol{X}_A - \boldsymbol{X}_B\|}. \tag{5}$$

The swelling of an object is modeled by increasing the natural spring length L_{AB} used in the mass-spring model in Eq. (3). As it can be seen in Fig. 3 (a), the natural length of the spring L_{AB}^{n+1} is a function of time, which depends on the characteristics of the solid object.

As the value of L_{AB} increases, the restoring force of the spring works and pull the position of the mass points to the new location as shown in Fig. 3 (b). In the proposed method, the objects are assumed to absorb surrounding water at the same rate as the swelling process. In addition, the objects are completely submerged within a closed system. The density of the object is assumed to be constant. Another important point to be noted is that as the objects swell, the distances between CDS increase and create empty spaces which allow objects to infiltrate each other during contact. In order to avoid this condition, the CDS radiuses are set to increase in the same rate as the increase of the

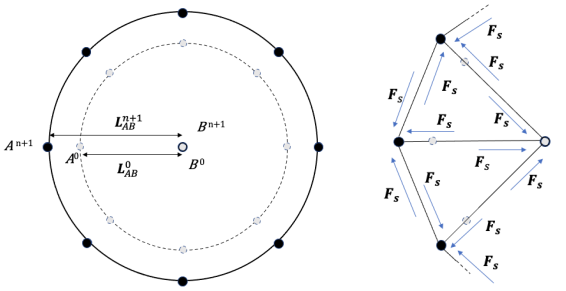

(a) Swelling scheme of an object (b) Free body diagram of the spring forces due to swelling

Fig. 3 (a) Proposed swelling scheme of an object and (b) its free body diagram

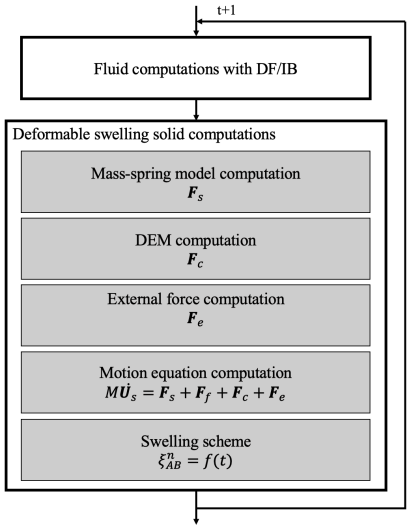

Fig. 4 Flowchart of the swelling deformable solid computation

natural spring length. The flowchart for the swelling deformable solid computations can be seen on Fig. 4.

3. APPLICATIONS

(1) Experiment and Computation on Swelling Behavior of Hydrogel Particles

In this section, the diameter growth of hydrogel particles is experimentally observed and implemented into the proposed method. The computation is conducted to confirm that as the swelling function is introduced, the used mass-spring model will not affect the swelling of the solid object. The hydrogel particles are spherical and made of a type of superabsorbent polymer (SAP) called sodium polyacrylate. A total of twenty hydrogel particles with three colors are put inside the water as shown in Fig. 5.

The particles are allowed to swell for around 10 [hrs] until they are saturated and reach their maximum sizes. The black colored hydrogel particles are easier to be seen, and, the distribution on the maximum sizes is more uniform than the other colors. For those

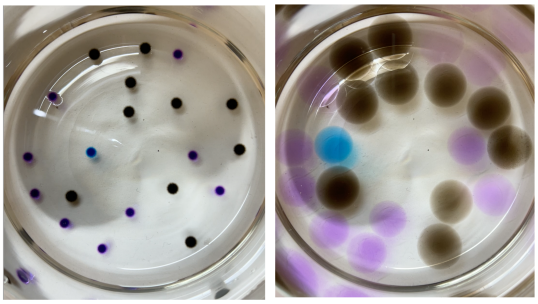

(a) t = 0.0 [hrs] (b) t = 9.7 [hrs]

Fig. 5 Experiment of hydrogel particles in water

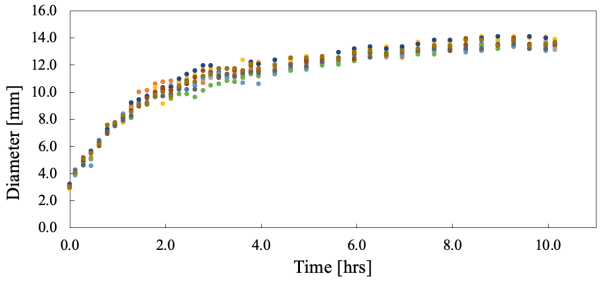

Fig. 6 Observed size growth of hydrogel particles (different colors indicate different black particles)

reasons, the swelling behavior of the black hydrogel particles are chosen to be used in the computation. The diameter of black particles are measured, and the growths are recorded as shown in Fig. 6.

As it can be seen, the black hydrogel particles grow more than triple in size from the initial diameter of around 3 [mm] within 2 [hrs] and the growth rate slowly decreases and the particles reach a stable size at around 13.5 [mm] after around 9 [hrs]. In addition, a regression analysis is performed using computer software (KaleidaGraph 4.5) and the relation between time (t) and diameter of the particles (D) is found. The equation for the relation of t and D for $0.0 \leq t \leq 9.7$ [hrs] is shown in the Eq. (6).

$$\begin{aligned} D = &-4.38 \times 10^{-26} t^6 + 5.88 \times 10^{-21} t^5 \\ &-3.36 \times 10^{-16} t^4 + 1.04 \times 10^{-11} t^3 \\ &-1.85 \times 10^{-7} t^2 + 0.002t + 2.98 \end{aligned} \quad (6)$$

The obtained Eq. (6) is used to calculate the change of the natural length of the spring L_{AB}^n. In the computation, a stationary particle with the initial diameter of 3 [mm] is set up within a computation area of 30 [mm] ×30 [mm]. Since the focus is on the swelling computation, the fluid and contact forces computation is omitted. The mass points number N_l as 20 is used, with the spring constant of mass-spring model $k_s = 10^6$ [N/m] and coefficient of restitution $e_s = 1.0$. Additionally, the solid density ρ_s as 1500 [kg/m^3] is used. The model is calculated with $\Delta t = 5 \times 10^{-3}$ [s]. Figure 7 shows the computation of a single hydrogel particle with the proposed method.

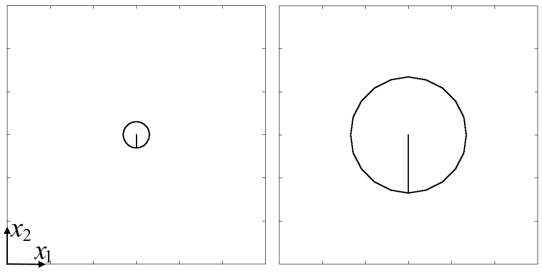

(a) t = 0.0 [hrs] (b) t = 9.7 [hrs]

Fig. 7 Computation of a single hydrogel particle (outline of the particle, with additional single line to check for rotation)

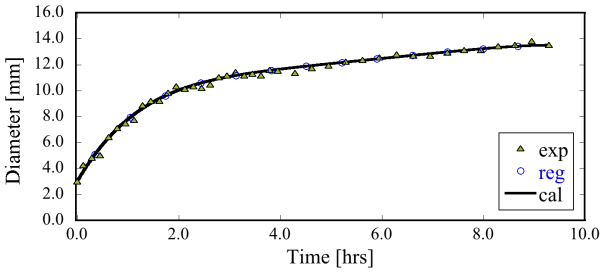

Fig. 8 Computed diameter of hydrogel particle (cal) compared to experiments (exp) and predicted results (reg)

The 20 mass points used in the computation are connected to represent the surface of the object, with the additional line to the center point to distinguish the rotation movements of the objects in the computation. The figures show the initial (t = 0.0 [hrs]) and final (t = 9.7 [hrs]) diameter of the hydrogel particle as 3 [mm] and 13.5 [mm] respectively. Additionally, no rotation on the particle can be observed.

Figure 8 shows the comparison between experimental data (exp), expected growth from regression analysis (reg), and the calculated results (cal). The diameter in the calculated results is obtained by averaging the distances of mass points on the boundary to the mass point on the center. The calculated results show that the object grows quickly with a smooth curve from the initial diameter until around 2 [hrs], then slowing down until it reaches the stable size of around 13 [mm], showing a good agreement with the experimental data and the expected growth from Eq. (6). In addition, two values of N_l are computed to check the convergences. Between the two values of N_l = 10 and N_l = 20, it can be seen that there are almost no differences as shown in Fig. 9.

(2) Sedimentation of a Single Particle in Fluid

It is to be emphasized that the proposed method is using a different DF/IB computation. Compared to the original DF/IB for rigid bodies, in which the total force of the Lagrangian points is calculated, and used to update the movement of the center point, the proposed method uses the interaction forces on each

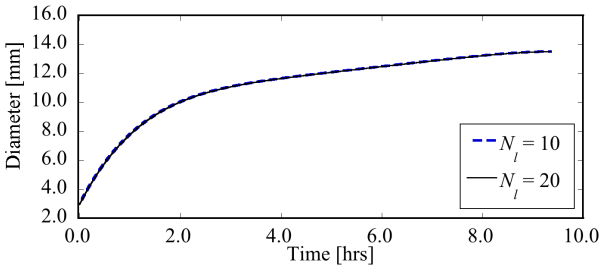

Fig. 9 Effects of Lagrangian Points number N_l on the time histories of diameter of hydrogel particle

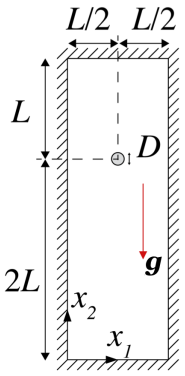

Fig. 10 Computational area for sedimentation of a single particle

point to update the motion separately. This method allows the deformations of the objects to be predicted. As the first step, it is important to confirm that the proposed method will give the same results as the original DF/IB for rigid bodies. the proposed method is applied to a case of sedimentation of a single particle in fluid.[24),25)]

A single particle with diameter D = 0.25 and density ρ_s = 1.25 is set inside a 2×6 area from the initial position of (1, 4) and falls freely with the gravity acceleration of -980 as shown in Fig. 10. The number of fluid cells N_f used in the computation is 200×600 and the number of Lagrangian points N_l is 70. The surrounding sides are treated as non-slip boundaries. The fluid density ρ_f and kinematic viscosity ν are 1.0 and 0.1 respectively, The spring constant and coefficient of restitution of mass-spring model k_s and e_s used are 4×10^6 and 1.0. A large enough k_s is used so that the solid doesn't deform and acts similar to a rigid body. The spring constant for the DEM calculation $k_{D,n} = k_{D,t} = 1 \times 10^4$ and coefficient of restitution for the DEM calculation e_D = 1.0 are used. The value of DEM parameters for contact between multiple gravel particles in the previous study by Ushijima is used as reference.[26)] The radius of the contact detection spheres is $0.2D$. The model is calculated with $\Delta t = 5 \times 10^{-3}$. It is to be noted that non-dimensional parameters are used.

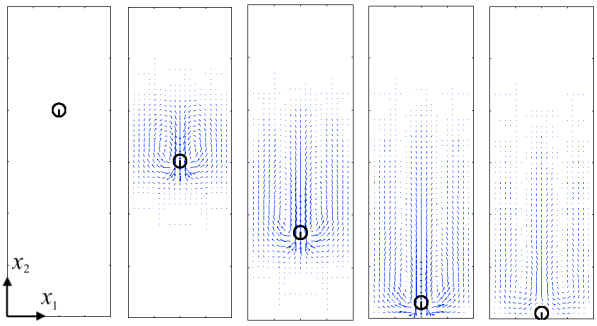

(a) $t = 0$ (b) $t = 0.25$ (c) $t = 0.50$ (d) $t = 0.75$ (e) $t = 1.00$

Fig. 11 Sedimentation of a single particle with MSM-DF/IB (velocity vectors and particle outline)

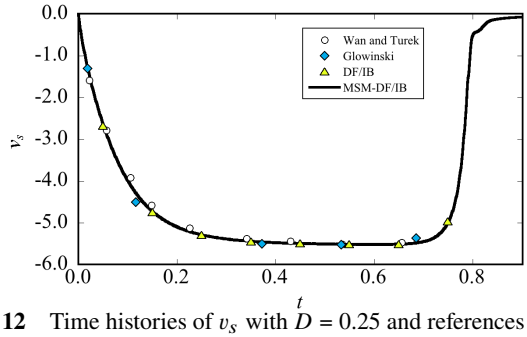

Fig. 12 Time histories of v_s with $D = 0.25$ and references

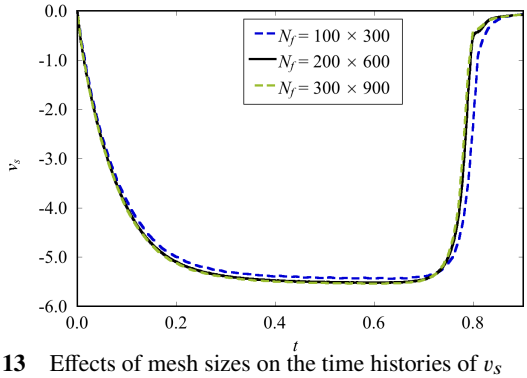

Fig. 13 Effects of mesh sizes on the time histories of v_s

The calculated value of particle velocity in y-direction v_s is observed and compared to the computation with original DF/IB for rigid body and past references.[24),25)] Figure 11 shows the computation of the sedimentation of a single particle.
The object is shown in the initial position (1,4) and falls straight to the bottom side of the computational area. Some velocities inside the objects can be observed. DF/IB method only overwrite the velocity of the boundary, leaving the velocity of the imaginary fluid inside the solid. It is to be noted that the velocity inside of the fluid has no effects on the solid movements.

Figure 12 shows the time histories of v_s. As the particle falls from the initial position, the velocity increases until it reaches the terminal velocity with $|v_s|$ around 5.5 at $t = 0.3$ until the object moves closer

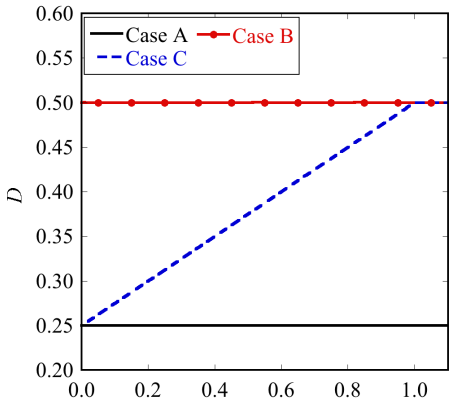

Fig. 14 Diameter of particles for case A, B, and C with respect to time

to the bottom side of the computational area and the $|v_s|$ decreases until to zero and settles there. The time histories of velocity from the proposed method give a good agreement with the original DF/IB method and references.

In order to check for the mesh convergence, the computation is checked for different N_f. In addition to the previous computation, a rougher resolution with $N_f = 100 \times 300$ and finer resolution with $N_f = 300 \times 900$ is computed. The results of the three computations can be seen on Fig. 13. It is shown that the computation is able to reach good results even at rougher mesh resolution, with more accurate results at mesh number 200×600 and the number of cells inside solid at around 25.

In addition to the computation, the sedimentation of a swelling particle is calculated. The diameter of the object increases linearly from $D = 0.25$ to the maximum size $D = 0.50$ linearly with slope = 0.25 or can be written as

$$D = \begin{cases} 0.25t + 0.25, & 0.0 \le t < 1.0 \\ 0.50, & t \ge 1.0. \end{cases} \tag{7}$$

In order to confirm the results of the maximum size of the swelling particle, another case with constant D = 0.50 is calculated. For convenience, the case with $D = 0.25$ calculated previously will be called case A, the case with $D = 0.50$ as case B, and the case with a swelling particle in which the diameter changes from the $D = 0.25$ to 0.50 as case C. The relation between the time and diameter of the three cases can be seen in Fig. 14. Other computational parameters used in the additional two cases are the same as case A.

The velocity vector and particle outline of the three cases can be seen in Figs. 15, 16 and 17. When $t = 0.00$, the three particles are setup in the same position and dropped. At $t = 0.25$, the particle in case B with largest initial diameter size and mass is the closest to the bottom than the particles in cases A and C. In addition, in this time step, the position of the object in

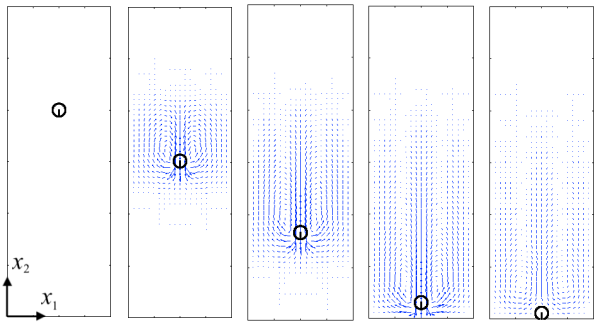

(a) $t = 0$ (b) $t = 0.25$ (c) $t = 0.50$ (d) $t = 0.75$ (e) $t = 1.00$

Fig. 15 Sedimentation of a single particle in fluid for case A (velocity vectors and particle outline)

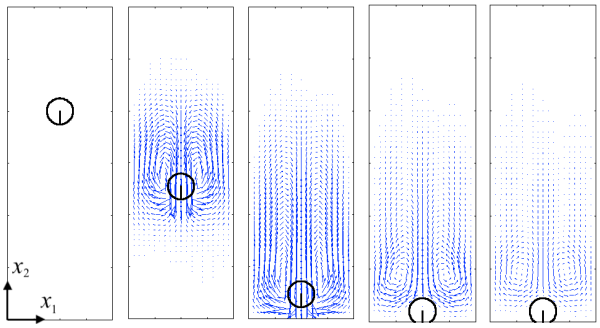

(a) $t = 0$ (b) $t = 0.25$ (c) $t = 0.50$ (d) $t = 0.75$ (e) $t = 1.00$

Fig. 16 Sedimentation of a single particle in fluid for case B (velocity vectors and particle outline)

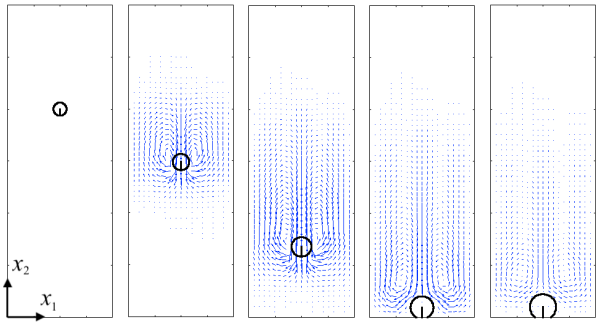

(a) $t = 0$ (b) $t = 0.25$ (c) $t = 0.50$ (d) $t = 0.75$ (e) $t = 1.00$

Fig. 17 Sedimentation of a single particle in fluid for case C (velocity vectors and particle outline)

cases A and C is similar as only small swelling occur to the particle in case C. At $t = 0.50$, the particle in case B almost hits the bottom. The diameter of the particle in case C is larger than the previous time step, and the position is closer to the bottom than in the case A. In the next time step at $t = 0.75$, the particles on cases B and C hit the bottom. The diameter of the particle in case C is around 0.438. At $t = 1.0$, all three particles settle on the bottom. The particle in case C can be seen on the bottom with diameter $D = 0.50$.

The v_s obtained in the three cases are compared in Fig. 18. The time history of v_s shown by the black solid line for the case A is the same as the one com-

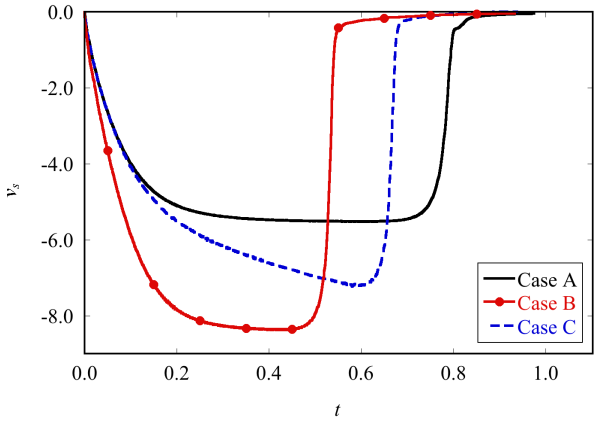

Fig. 18 Time histories of particle velocity v_s for case A ($D = 0.25$), case B ($D = 0.5$), and case C ($D = 0.25$ to 0.50)

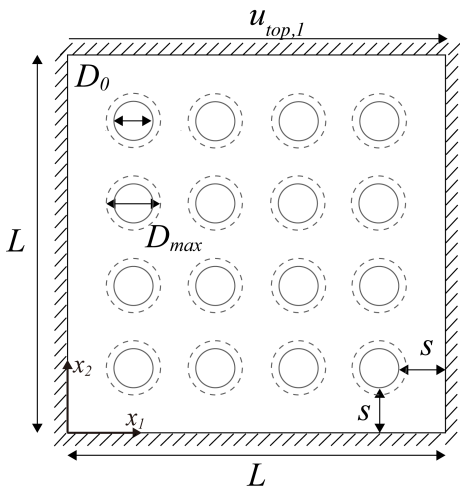

Fig. 19 Computational area with swelling deformable objects

puted previously in Fig. 12 In case B, as the size and mass of particle are larger than the case A, the terminal velocity is larger, obtained at $|v_s|$ around 8.3 at t = 0.2.

In the case C, the particle falls from the initial position with initial diameter $D = 0.25$. As the particle's diameter and mass increase, the $|v_s|$ also increases continuously without reaching the terminal velocity. The swelling particle hits the bottom side with a diameter $D = 0.438$. From Fig. 12, the time history of the velocity for the swelling particle at case C fits between cases A and B where the minimum and maximum diameter of the swelling particle is used, showing reasonable results for the computation.

(3) Lid-Driven Cavity Flow with Multiple Swelling Objects

Multiple deformable solid objects are arranged inside the 2D computational area filled with the fluid as shown in Fig. 19.

The computational area is a square with the length

$L = 1.0$. Initially, 16 objects with the initial diameter $D_0 = 0.12$ and solid density $\rho_s = 1500$ are set up inside the computational area with space between objects and wall s as 0.104. For the fluid, kinematic viscosity $\nu = 0.01$ and fluid density $\rho_f = 1000$ are used. The surrounding walls are treated as non-slip boundaries. The top wall moves in horizontal direction with velocities $u_{top,1} = 0.1$ and $u_{top,2} = 0$ and other walls are stationary. The Reynolds number $\mathrm{Re} = u_{top,1}L/\nu$ is 10, and the number of fluid cells N_f used is 100×100. The number of mass points (Lagrangian points) N_l is 21. In this resolution, the number of cells inside objects become around 12 before swelling, and 18 after swelling. This resolution is similar to the previous application with rougher mesh. Two different values of k_s are used in this application, $k_s = 1000$ for case 1 and $k_s = 100$ for case 2. Additionally, coefficient of restitution e_s for the two cases are 1.0. For the DEM calculation, the values of $k_{D,n}$ and $k_{D,t}$ in both cases are 1.0×10^4 with the coefficient of restitution $e_D = 1.0$, and the radius of the contact detection spheres is $0.2D$. Time increment $\Delta t = 5.0 \times 10^{-3}$ is used.

The objects are set to swell linearly with the slope of 6×10^{-4}, until the maximum size D_{max} of 0.18. The relation between t and D can be written as Eq. (8)

$$D = \begin{cases} 6 \times 10^{-4} t + 0.12, & 0 \le t < 100 \\ 0.18, & t \ge 100. \end{cases} \tag{8}$$

The computations of swelling deformable objects on two cases with two spring constant values of mass-spring model $k_s = 1000$ and $k_s = 100$ can be seen in Figs. 20 and 21.

At first, the horizontal velocity to the right side on the top wall causes the circulating flow in the clockwise direction on the top half of the computation area. The solid objects are transported by the fluid flows while rotating individually. The fluid flow causes deformations on the objects as it can be seen on the area closer to the moving top wall where the fluid force is stronger. As the objects move, they also make contact with the surrounding objects and the walls. The solid-solid and solid-wall contacts causes further deformations on the solid objects. Larger deformations can be observed on the case 2 where smaller k_s value is used. Additionally, as the objects are moving, the diameter of the objects increases with the introduced swelling condition. As the objects swell, the computational area is filled with the objects and slower movements can be observed as seen in the flow velocity vector distribution on Figs. 20 and 21 when $t = 110$. In both cases, the fluid flow do not reach a steady state.

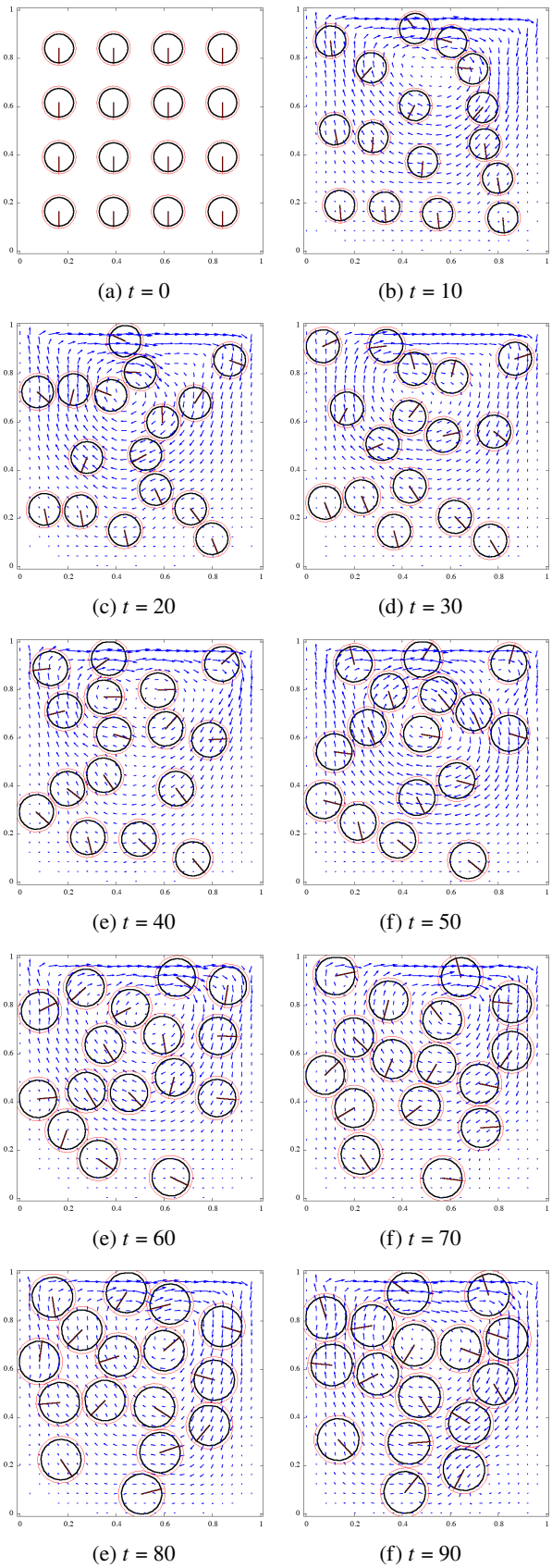

(a) $t = 0$ (b) $t = 10$ (c) $t = 20$ (d) $t = 30$ (e) $t = 40$ (f) $t = 50$ (e) $t = 60$ (f) $t = 70$ (e) $t = 80$ (f) $t = 90$

Fig. 20 Cavity flow with deformable swelling objects (velocity vectors (blue), object outlines (black), and CDS outer line (red)) with $k_s = 1000$

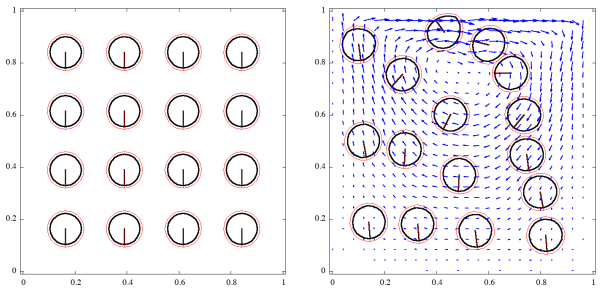

(a) t = 0 (b) t = 10

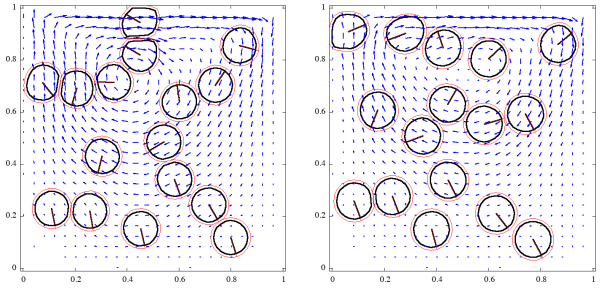

(c) t = 20 (d) t = 30

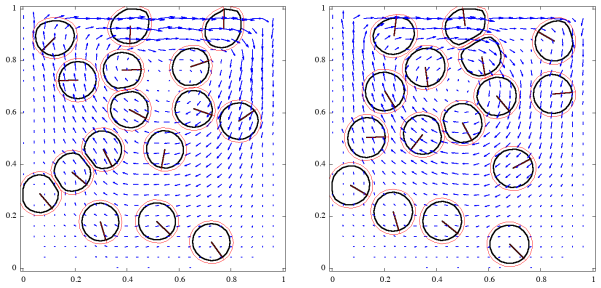

(e) t = 40 (f) t = 50

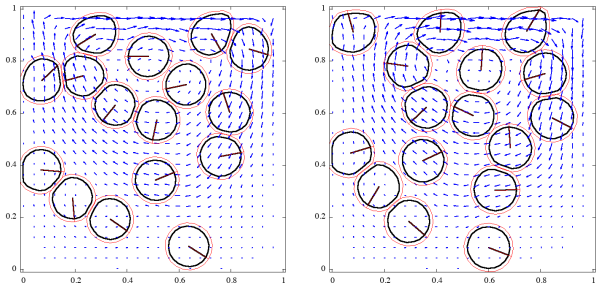

(e) t = 60 (f) t = 70

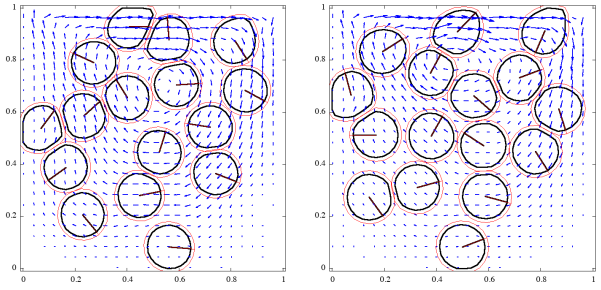

(e) t = 80 (f) t = 90

Fig. 21 Cavity flow with deformable swelling objects (velocity vectors (blue), object outlines (black), and CDS outer line (red)) with k_s = 100

4. CONCLUSIONS

In this study, a method has been proposed to simulate the interactions between fluid and deformable swelling solid using DF/IB and the mass-spring model.

The proposed method was applied to several different computations. First, an experiment on several hydrogel particles was conducted and the time histories of the diameter growth were recorded. A regression analysis was then conducted on the data and the equation for the relation between time and diameter was obtained and used in the proposed method to calculate a single hydrogel particle. The calculated results were then compared back to the experimental data and the regression equation. It is confirmed that the proposed method is able to give a good agreement to the observed swelling of hydrogel particles.

In the second application, the proposed method with a large spring stiffness value was compared to the original DF/IB method for rigid bodies by calculating the sedimentation of a single particle in fluid. By comparing the calculated particle velocity in y-direction v_s to the original DF/IB method for rigid bodies and references, it is confirmed that the proposed method gives a good agreement with the original DF/IB for rigid body and references. In addition, a case of sedimentation of a single swelling particle was calculated. A particle was dropped from the initial position with the minimum diameter inside fluid and as it fell to the bottom side of the computational area, the diameter D increases from 0.25 to 0.50. The value of v_s for the swelling particle was compared with the v_s of two cases of the sedimentation of a non-swelling particle with constant D = 0.25 and D = 0.50. Reasonable results can be observed as the time history of v_s in the computation of swelling object fits between the two other cases. It can also be observed that the computation with swelling particle never reached its terminal velocity as the object did not swell to the maximum diameter before hitting the bottom side of the computational area.

Finally, the proposed method is applied to the computation of lid-driven cavity flow with multiple swelling objects. In the computation, two values of k_s were investigated. The solid objects are transported by the fluid flows while rotating individually while the diameter slowly increases. Strong fluid flow, especially which can be seen close to the top wall causes the objects to deform. In addition, the solid-solid and solid-wall contacts causes further deformations. Larger deformations can be observed on the second case with smaller k_s. Furthermore, slower movements of the objects can be observed from the fluid velocity vector distribution as the size of the objects increases and filled the computational area. It was demonstrated

that the proposed method allows us to calculate deformations and swelling within fluid-solid interactions with reasonable results.

A detailed study on the deformation is considered for future works. Even though the proposed method are able to give reasonable results, there are several limitations and points that need to be improved. The spring parameters used in the applications are introduced to observe whether the proposed method are able to simulate the deformation on the objects. In addition, the spring constant of the solid objects are set to be constant in this paper. In reality, as objects size increase, it is possible that the stiffness change. Several experiments focusing on the deformations on the objects will be conducted and the acquired physical parameters such as spring constants k_s, and the change of k_s due to swelling will be used in the next step computations.

REFERENCES

1) Murad, M. A., and Cushman, J. H., 1996. "Multiscale flow and deformation in hydrophilic swelling porous media". *International Journal of Engineering Science,* **34**(3), pp. 313–338.
2) Saikhwan, P., Mercadé-Prieto, R., Chew, Y., Gunasekaran, S., Paterson, W., and Wilson, D., 2010. "Swelling and dissolution in cleaning of whey protein gels". *Food and Bioproducts Processing,* **88**(4), pp. 375–383. Special Issue on Fouling and cleaning in food processing 2010.
3) Javadov, S., Chapa-Dubocq, X., and Makarov, V., 2018. "Different approaches to modeling analysis of mitochondrial swelling". *Mitochondrion,* **38**, pp. 58–70.
4) Somers, M. J., Alfaro, J. F., and Lewis, G. M., 2021. "Feasibility of superabsorbent polymer recycling and reuse in disposable absorbent hygiene products". *Journal of Cleaner Production,* **313**, p. 127686.
5) Lenji, M. A., Haghshenasfard, M., Sefti, M. V., Salehi, M. B., and Heidari, A., 2018. "Experimental study of swelling and rheological behavior of preformed particle gel used in water shutoff treatment". *Journal of Petroleum Science and Engineering,* **169**, pp. 739–747.
6) Knaebel, A., Rebre, S., and Lequeux, F., 1997. "Determination of the elastic modulus of superabsorbent gel beads". *Polymer Gels and Networks,* **5**(2), pp. 107–121.
7) Jockusch, S., Turro, N. J., Mitsukami, Y., Matsumoto, M., Iwamura, T., Lindner, T., Flohr, A., and Massimo, G. D., 2009. "Photoinduced surface crosslinking of superabsorbent polymer particles". *Journal of Applied Polymer Science,* **111**, pp. 2163–2170.
8) Misiewicz, J., Glogowski, A., Lejcuz, K., and Marczak, D., 2020. "The characteristics of swelling pressure for superabsorbent polymer and soil mixtures". *Materials,* **13(22)**, p. 5071.
9) Diersch, H.-J., Clausnitzer, V., Myrnyy, V., Rosati, R., Schmidt, M., Beruda, H., Ehrnsperger, B., and Virgilio, R., 2010. "Modeling unsaturated flow in absorbent swelling porous media: Part 1. theory". *Transport in Porous Media,* **83**, pp. 437–464.
10) Diersch, H.-J., Clausnitzer, V., Myrnyy, V., Rosati, R., Schmidt, M., Beruda, H., Ehrnsperger, B., and Virgilio, R., 2011. "Modeling unsaturated flow in absorbent swelling porous media: Part 2. numerical simulation". *Transport in Porous Media,* **86**, pp. 753–776.
11) Sweijen, T., Chareyre, B., Hassanizadeh, S., and karadimitrou, N., 2017. "Grain-scale modelling of swelling granular materials; application to super absorbent polymers". *Powder Technology,* **318**, pp. 411–422.
12) Nagano, K., Toriu, D., and Ushijima, S., 2020. "Computational method for free-surface flows between multiple absorbent particles". *Journal of JSCE, Ser. A2 (Applied Mechanics),* **76**(2), pp. I˙109–I˙117.
13) Terzopoulos, D., Platt, J., Barr, A., and Fleischer, K., 1987. "Elastically deformable models". *ACM Siggraph Computer Graphics,* **21**, pp. 205–214.
14) Provot, X., 1995. "Deformation constraints in a spring-mass model to describe rigid cloth behavior". *Proceedings of Graphics Interface*, pp. 147–154.
15) Mongus, D., Repnik, B., Mernik, M., and Zalik, B., 2012. "A hybrid evolutionary algorithm for tuning a cloth-simulation model". *Applied Soft Computing,* **12**(1), pp. 266–273.
16) Xu, L., Lu, Y., and Liu, Q., 2018. "Integrating viscoelastic mass spring dampers into position-based dynamics to simulate soft tissue deformation in real time". *Royal Society Open Science,* **5**(2), p. 171587.
17) Najafabadi, A., Khanmirza, E., and Markazi, A., 2021. "Experimental study and modeling of soft body behavior based on the mass-spring-damper method". *2021 9th RSI International Conference on Robotics and Mechatronics (ICRoM)*, pp. 346–351.
18) Duan, Y., Huang, W., Chang, H., Chen, W., Zhou, J., Teo, S., Su, Y., Chui, C. K., and Chang, S., 2014. "Volume preserved mass-spring model with novel constraints for soft tissue deformation". *IEEE Journal of Biomedical and Health Informatics,* **20**(1), pp. 549–558.
19) Guinea, N., Toriu, D., and Ushijima, S., 2022. "Computational method for interactions between deformable objects and fluid flows using immersed boundary method and mass spring model". *Transaction of Japan Society for Simulation Technology,* **14**(2), pp. 1–7.
20) Guinea, N., Toriu, D., and Ushijima, S., 2022. "Numerical experiments of swelling objects interacting with newtonian fluids". *Proceedings of The 41st JSST Annual International Conference on Simulation Technology*, pp. 57–60.
21) Uhlmann, M., 2005. "An immersed boundary method with direct forcing for the simulation of particulate flows". *J. Comput. Phys.,* **209**, pp. 448–476.
22) Cundall, P., and Strack, O., 1979. "A discrete numerical model for granual assemblies". *Geotechnique,* **29**(1), pp. 47–65.
23) Ushijima, S., Toriu, D., Yanagi, H., and Tanaka, H., 2019. "Numerical prediction for transportation of gravel particles and saltation-collapse equilibrium due to vertical jet". *Journal of JSCE,* **75**, pp. 289–300.
24) Glowinski, R., Pan, T.-W., Hesla, T., and Joseph, D., 2001. "A fictitious domain approach to the direct numerical simulation of incompressible viscous flow past moving rigid bodies:application to particulate flow". *Journal of Computation Physics,* **169**, pp. 363–426.
25) Wan, D., and Turek, S., 2006. "Direct numerical simulation of particulate flow via multigrid FEM techniques and the fictitious boundary method". *International Journal of Numerical Methods Fluids,* **51**, pp. 531–566.
26) Ushijima, S., Toriu, D., Yanagi, H., and Yagyu, D., 2017. "Computations on transportations of gravel particles due to overflows taking account of particle-particle and particle-fluid mechanical interactions". *Journal of JSCE, Ser. A2 (Applied Mechanics),* **73(2)**, pp. I˙377–I˙386.

(Received June 24, 2022)
(Accepted November 30, 2022)